Journal of Catalysis 337 (2016) 91–101

Contents lists available at ScienceDirect

Journal of Catalysis

journal homepage: www.elsevier.com/locate/jcat

Preferential activation of CO near hydrocarbon chains during Fischer–Tropsch synthesis on Ru

David Hibbitts [a,b], Eric Dybeck [c], Thomas Lawlor [c], Matthew Neurock [c,d,*], Enrique Iglesia [a,*]

[a] Department of Chemical and Biomolecular Engineering, University of California, Berkeley, CA 94720, United States
[b] Department of Chemical Engineering, University of Florida, Gainesville, FL 32611, United States[1]
[c] Department of Chemical Engineering, University of Virginia, Charlottesville, VA 22904, United States
[d] Department of Chemical Engineering and Materials Science, University of Minnesota, Minneapolis, MN 55455, United States

ARTICLE INFO

Article history:
Received 25 November 2015
Revised 14 January 2016
Accepted 16 January 2016

Keywords:
Fischer–Tropsch synthesis
CO activation
C–C bond formation
Co-adsorbate interactions
Ruthenium
Coverage effects

ABSTRACT

We report here theoretical evidence for an enhancement in CO activation to form C_1 monomers at locations near growing hydrocarbon chains as a result of their ability to disrupt the dense monolayers of chemisorbed CO* present during Fischer–Tropsch synthesis (FTS). These previously unrecognized routes become favored at the high CO* coverages that prevail on curved cluster surfaces at conditions of FTS practice and account for the rapid growth of chains, which requires a source of vicinal monomers. CO activation initially requires a vacant site (and consequently CO* desorption) and proceeds via CO* reactions with H* to form hydroxymethylene (CH*OH*), which then dissociates to form OH* and CH*; CH_x* species can subsequently act as monomers and insert into chains, a process denoted as the 'carbene' mechanism. These CH*, and their larger alkylidyne (C_nH_{2n-1}*) homologs, disrupt the dense CO* adlayers and in doing so allow the facile formation of vicinal CH*OH* intermediates that mediate CO activation, without requiring, in this case, CO* desorption. This causes CO* activation effective enthalpy and free energy barriers to be ~100 and ~15 kJ mol^{-1} lower, respectively, near growing chains than within unperturbed monolayers. These effects are observed near alkylidyne (C_nH_{2n-1}*) but not alkylidene (C_nH_{2n}*) or alkyl (C_nH_{2n+1}*) chains. These phenomena cause monomers to form preferentially near growing alkylidyne chains, instead of forming at undisrupted regions of CO* monolayers, causing chain growth (via CH_x*-insertion) to occur much more rapidly than chain initiation, a requirement to form long chains. Such routes resolve the seemingly contradictory proposals that CH_x* species act as monomers (instead of CO*) and chain initiators, but their formation and diffusion on dense CO* adlayers must occur much faster than chain initiation for such chains to grow fast and reach large average lengths. Chains disrupt surrounding molecules in the adlayer, causing faster monomer formation precisely at locations where they can readily react with growing chains. This work illustrates how interactions between transition states and co-adsorbates can dramatically affect predicted rates and selectivities at the high coverages relevant to practical catalysis.

Published by Elsevier Inc.

1. Introduction

Fischer–Tropsch synthesis (FTS) converts synthesis gas mixtures (CO and H_2) to hydrocarbons on Fe, Co, and Ru catalysts [1–3]; it is a process critical to the success of many strategies for the conversion of natural gas, biomass, and CO_2 to fuels, energy carriers, and chemicals. Hydrocarbon chains are initiated by CO activation on metal surfaces; these chains propagate by adding CO-derived monomers and terminate via desorption as alkenes, alkanes, and mixtures of oxygenates [2–4]. Kinetic [5–7], infrared [8,9], isotopic switch [4], and theoretical studies [8] indicate that these reactions occur on surfaces nearly saturated with chemisorbed CO (CO*).

Recent studies have confirmed that CO activation occurs via H-assisted routes that form hydroxymethylene (CH*OH*) species before the cleavage of the C–O bond on Co and Ru [6,8,10,11]. CH*OH* dissociates to form CH* species that hydrogenate to form CH_x* (and ultimately CH_4) or react with a CO*-derived monomer (C_1*, CO* or CH_x*) to form C–C bonds; the OH* formed via CH*OH* dissociation results in H_2O co-products [6,8,10–12]. Such

* Corresponding authors at: Department of Chemical Engineering, University of Virginia, Charlottesville, VA 22904, United States.
E-mail addresses: mneurock@umn.edu (M. Neurock), iglesia@berkeley.edu (E. Iglesia).
[1] Present address.

http://dx.doi.org/10.1016/j.jcat.2016.01.010
0021-9517/Published by Elsevier Inc.

mechanistic consensus is not apparent for C–C bond formation routes. $^{12}CO/^{13}CO$ isotopic switch data have shown that alkenes form with similar isotopic content at each location along the backbone, indicating that all of its C-atoms are added within a period of time much shorter than the time required to replace CO* reactant with a given carbon isotope [4]. These data indicate that a small number of chains grow rapidly on surfaces during FTS, via a process that appears to require the rapid formation of monomers within diffusion distances from growing chains.

Hydrocarbon chains can react with vicinal CO* in CO-insertion routes that form C–C bonds and CH_xCO^* species; the latter may desorb after H-addition to form alkanals and alkanols or cleave its C–O bond to form precursors to alkenes and alkanes [13–18]. The rapid chain growth processes discussed above could plausibly occur via CO*-insertion because of readily available vicinal CO* when chains grow on CO*-saturated surfaces; theoretical treatments of such routes will be reported in a separate manuscript at a later time.

CH_x^* addition to growing chains can also form C–C bonds, as inferred from the incorporation of CH_2^* species derived from CH_2N_2 into the hydrocarbons formed from H_2–CO reactants [19,20], via a process that has been denoted as the carbene route [21–26]. These CH_x^* species form from CO* via the same H*-assisted CO cleavage that initiates chains. For fast chain growth [4], such CH_x-insertion propagation routes would require that CO activation steps be much faster than the corresponding steps that initiate chains and that CH_x^* species, some with multiple covalent surface attachments, diffuse very rapidly on CO*-saturated surfaces.

Here, we provide theoretical evidence for an alternate route that involves the preferential H-assisted activation of CO* molecules that reside next to a growing chain. Such processes are made possible through a disruption of dense CO* monolayers by such growing chains, which lead to an "activation space"; this space avoids the need to desorb an additional CO*, which carries a significant enthalpic penalty, to ameliorate the repulsive forces that destabilize transition states at high CO* coverages. These first-principles density functional theory (DFT) calculations show that enthalpy and free energy barriers for H*-assisted CO* activation on Ru surfaces are lower for activating CO* vicinal to hydrocarbon chains, via monolayer disruption phenomena that are likely to prevail at the CO* coverages required for significant chain growth from H_2–CO reactants on other FTS catalysts. These seemingly unrecognized processes allow fast CH_x^* mediated chain propagation to readily occur via preferential monomer formation near growing chains and thus account for the rapid chain growth observed experimentally but inconsistent with the carbene route. More generally, the results presented herein indicate that dense adlayers, ubiquitous in the practice of catalysis, significantly influence the steric and electronic properties of sites and intermediates and thus the reactivity of adsorbates, an essential feature often ignored in fundamental studies carried out on model surfaces at low surface coverages.

2. Methods

Periodic plane-wave DFT methods implemented in the Vienna *ab initio* simulation package (VASP) [27–30] were used to calculate adsorption and reaction energies and activation barriers for elementary steps involved in CO* activation and CH_x^* formation. Plane-waves were constructed using projector augmented-wave (PAW) potentials with an energy cutoff of 400 eV [31,32]. The revised Perdew–Burke–Ernzerhof (RPBE) form of the generalized gradient approximation (GGA) was used to determine exchange and correlation energies [33–35]. Furthermore, calculations were carried out using optB86b-vdW [36] and vdw-DF2 [37] GGA functionals to describe dispersion forces among atoms. Similar dispersive interactions were incorporated into RPBE calculations using DFT-D3 with Becke and Johnson (BJ) damping [38,39]. DFT-D3 was also used to determine interactions among non-metal atoms (C, O, and H) to correct for dispersive interactions only between co-adsorbates, as the parameters for the DFT-D3 method were primarily based on interactions of gas-phase species [38,39]. Wavefunctions were converged to within 10^{-6} eV and forces were computed using a fast Fourier transform (FFT) grid with a cutoff of twice the planewave cutoff. A $1 \times 1 \times 1$ Monkhorst–Pack sampling of the first Brillouin zone (k-point mesh) was used [40] and structures were relaxed until forces on unconstrained atoms were <0.05 eV/Å.

A 586-atom Ru cubo-octahedral particle (~2.5 nm in diameter) was used in the calculations at 1.044 CO*/Ru coverages (284 CO* on 272 surface Ru atoms) to account for sites with different coordinations and relevant CO* coverages. Edge and corner atoms of low coordination (96 atoms) on Ru_{586} stabilized bridge-bound CO* species (108 CO* species) that lead to supramonolayer coverages (Fig. 1) through the formation of geminal dicarbonyl species as observed with infrared experiments [8]. The high saturation coverages found here are fully consistent with in situ infrared studies [8,9,41], isotopic switch experiments [4], transient kinetic studies [6] and previous FTS kinetic studies [5–7] that all indicate that the Co and Ru surfaces are fully covered in CO* at FTS conditions. CO* peak intensities measured on Ru with in situ infrared spectroscopy no longer increase with increasing CO pressures above ~0.5 kPa CO even at higher temperatures (548–598 K) than those associated with FTS (~500 K), indicating that surfaces are saturated at such pressures [41]. Furthermore CO hydrogenation rates on Ru obtained at near-methanation conditions (548–598 K and 0.01–10 kPa CO) show that hydrogenation becomes inhibited by CO (indicating CO* coverages exceed 0.5 ML) at less than 0.1 kPa CO [41]. This is consistent with high-vacuum studies that indicate saturation coverages of ~0.9 ML CO* are reached at 10^{-2} Torr [42]. Rigorous FTS kinetic studies on Ru [8] and Co [6] also show that the rates of FTS are inhibited by increasing CO pressure which is a direct result of the dominance of the $K_{CO}(CO)$ term in the denominator of the rate equation:

$$r = \frac{\alpha(H_2)(CO)}{[1 + K_{CO}(CO)]^2}$$

At conditions typical of FTS, the surface is fully covered in CO* and thus $K_{CO}(CO)$ is $\gg 1$, leading to rates inversely proportional to CO pressure:

$$r = \frac{\alpha'(H_2)}{K_{CO}(CO)}$$

The bottom six layers of the Ru_{586} cluster were removed along the (1 1 1) surface and the bottom two layers of this structure and their CO* species were not allowed to relax during the calculations in order to decrease the computational demands and thus be able to explore a wider range of plausible intermediates and routes (Fig. 1). This Ru_{218} polycrystalline model was used for all calculations reported.

Transition state structures obtained for elementary steps were explored using nudged elastic band (NEB) methods [43,44] and then refined using dimer methods [45]. NEB methods used 16 images and wavefunctions converged to 10^{-4} eV with a FFT grid 1.5 times the size of the plane-wave cutoff. Maximum forces on each atom were converged to <0.3 eV/Å. The dimer algorithm was then used with wavefunctions converged to $<10^{-6}$ eV and a FFT grid size twice the planewave cutoff and converged to a maximum force of <0.05 eV/Å on each atom.

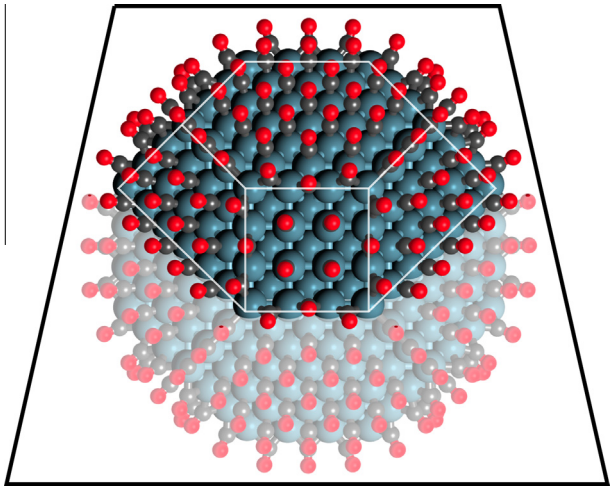

Fig. 1. Ru_{586} nanoparticle at 1.044 ML CO* along with the (1 1 1) plane used to cleave the catalyst model into a more computationally-feasible Ru_{218} structure with four metal layers orthogonal to the closed-packed terrace.

Frequency calculations were carried out on all optimized states to determine zero-point vibrational energies (ZPVE), vibrational enthalpies (H_{vib}), and free energies (G_{vib}). Their values were used, together with VASP-derived electronic energies (E_0), to obtain enthalpies:

$$H = E_0 + \text{ZPVE} + H_{vib} + H_{trans} + H_{rot} \quad (1)$$

and free energies:

$$G = E_0 + \text{ZPVE} + G_{vib} + G_{trans} + G_{rot} \quad (2)$$

for all reactant, product, and transition state structures. For RPBE GGA, the dispersion-corrected enthalpies:

$$H = E_0 + E_d + \text{ZPVE} + H_{vib} + H_{trans} + H_{rot} \quad (3)$$

and free energies:

$$G = E_0 + E_d + \text{ZPVE} + G_{vib} + G_{trans} + G_{rot} \quad (4)$$

were also calculated, where E_d is the dispersive energy between all C, O, and H atoms estimated by DFT-D3(BJ) methods [38,39]. For gaseous molecules, translational and rotational enthalpies and free energies were computed from statistical mechanics. The equations used to determine ZPVE, H_{vib}, and G_{vib} from vibrational frequencies for all species and H_{trans}, H_{rot}, G_{trans}, and G_{rot} from statistical mechanics formalisms for gas-phase molecules are reported in the Supporting Information (SI; Eqs. (S1)–(S13)).

3. Results and discussion

3.1. Theoretical treatments of dense monolayers of chemisorbed CO on Ru particles

The construction and analysis of relevant surfaces and of the elementary steps that they mediate require that we consider the number, configurations and binding energies of the CO* species that form the monomers involved in chain growth and that we do so on surfaces with CO* coverages of practical interest. Particle models allow for a more rigorous examination of the effects of surface atom coordination and of surface and adsorbate relaxations without the unphysical lateral rigidity imposed by flat extended models [8,10]. FTS turnover rates on Co [2,46] and Ru [47] catalyst increase with increasing particle size and then reach constant values for particles larger than 10 nm, indicating that turnovers occur predominantly on low-index planes that prevail on larger particles. Smaller particles contain significant fractions of defect sites that can activate CO* to form strongly-bound C* and O* species which ultimately deactivate such particles and may lead to bulk oxidation [2]. DFT-calculated differential CO adsorption enthalpies and free energies ($\Delta H_{ads,CO}$ and $\Delta G_{ads,CO}$ (at 1 bar) without dispersion corrections) on low-index terraces of the Ru_{218} particles at 1.044 CO* ML coverages are −46 kJ mol^{-1} and +36 kJ mol^{-1} (at 500 K), respectively (Fig. 2). The positive $\Delta G_{ads,CO}$ values would preclude CO* adsorption at these coverages even at the high CO pressures of FTS (~10 bar CO). These positive adsorption free energies reflect strong CO*–CO* repulsions, which are depicted visually in Fig. 2 by the overlapping van der Waals radii on such crowded surfaces.

These DFT-derived energies, however, neglect dispersive CO*–CO* interactions and thus underestimate attractive induced dipole interactions between CO* adsorbates, which, if included, stabilize CO* species. These attractive forces are considered here by using empirical (DFT-D3) [38,39] and semi-empirical (optB86b-vdW [36] and vdW-DF2 [37] exchange correlation functionals) methods. These methods substantially lower the $\Delta H_{ads,CO}$ and $\Delta G_{ads,CO}$ values (by 21–124 kJ mol^{-1}) relative to those from RPBE methods on surfaces with 1.044 ML CO*, but do not detectably influence adsorption entropies ($\Delta S_{ads,CO}$; Table 1). DFT-D3 methods give the strongest stabilization (decreasing both $\Delta H_{ads,CO}$ and $\Delta G_{ads,CO}$ by 123 kJ mol^{-1}); while this empirical method can effectively model non-covalent interactions between gas-phase molecules [38,39], it has not been parametrized for the interactions between adsorbates and surface Ru atoms. Therefore, we include only dispersive interactions among co-adsorbates (non-metal atom interactions (NMI)); RPBE-D3(NMI) gives $\Delta H_{ads,CO}$ and $\Delta G_{ads,CO}$ values of −106 kJ mol^{-1} and −23 kJ mol^{-1} at 500 K, which are well within the range given by the other DFT methods such as PW-91/USPP and PBE/PAW methods used elsewhere [12–15,20], but are derived from methods which do not 'overbind' CO* at low-coverages as PW-91 and PBE approaches do (Table 1) [35,48,49]. Also, the $\Delta H_{ads,CO}$ and $\Delta G_{ads,CO}$ values from RPBE-D3(NMI) are consistent with the high CO* coverages detected by infrared spectroscopy [8,9,41], isotopic switch experiments [4], and kinetic data [5–7] at the conditions of FTS catalysis, as further discussed in Section 2. All enthalpies and free energies henceforth include E_d values estimated by D3(NMI) methods, using Eqs. (3) and (4) in Section 2, and all calculations are carried out within these dense monolayers on Ru_{218} particles (1.044 ML CO*).

3.2. Chain initiation processes on CO*-covered surfaces

We examine here how the presence of hydrocarbon chains disrupts these CO* monolayers and, in doing so, influences H*-assisted CO* activation transition states. H-assisted CO* activation requires quasi-equilibrated steps that form vacancies (via CO* desorption, reverse of Step 1 in Scheme 1), CH*O* (via H-addition to CO*, Step 3) and CH*OH* (via irreversible H-addition to CH*O*, Step 4), which dissociate to CH* and OH* (Step 5) that end up being removed as part of a chain and H_2O products, respectively (Scheme 1). H_2 dissociation (Step 2) requires vacant metal atoms for its transition state, but at equilibrium, chemisorbed H-atoms (denoted as H′) reside at three-fold sites within the dense CO* adlayer and do not displace co-adsorbed CO*. The presence of H′ at a three-fold site vicinal to CO* increases $\Delta G_{ads,CO}$ values from −23 kJ mol^{-1} to −13 kJ mol^{-1} (500 K), an amount that is not sufficient to prevent CO* adsorption at such sites at the CO pressures typical of FTS (10 bar CO).

The inability of H′ to displace CO* at low H′ coverages is reflected in IR studies [6,8,9,41] that show CO* peak intensities that are independent of H′ coverage. This is also consistent with large free energies for dissociative H_2 chemisorption (~40 kJ mol^{-1}) and low barriers for associative H′ desorption (~20 kJ mol^{-1})

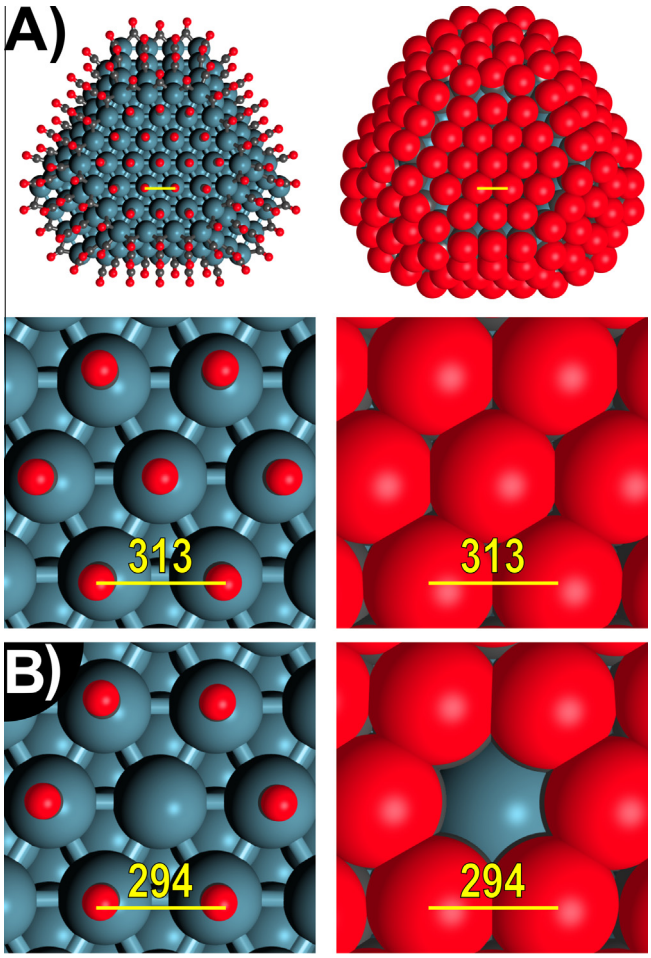

Fig. 2. Calculated structures for (A) CO*-covered Ru_{218} particles and (B) vacancies at the center of the (1 1 1) terrace of Ru_{218} particles with views (on right) illustrating the crowded nature of these surfaces by displaying atoms with their van der Waals radii. O–O bond distances between neighboring CO* adsorbates are given in pm. Differential adsorption enthalpies ($\Delta H_{ads,CO}$, kJ mol^{-1}), entropies ($\Delta S_{ads,CO}$, J mol^{-1} K^{-1}), and free energies ($\Delta G_{ads,CO}$, kJ mol^{-1}) for CO* are shown with (D3(NMI)) and without (RPBE) dispersion corrections.

which indicate quasi-equilibrated hydrogen adsorption. The low coverage of H′ is also supported by a range of other kinetic studies that show FTS rates that are linearly proportional to H_2 pressure at all relevant H_2 pressures [2,5–8,10].

H*-assisted CO* activation routes (Scheme 1) lead to a FTS rate equation consistent with reported rate data [2,5–8,10]:

$$r = \frac{\gamma K_{CO}(CO)(H_2)}{[1 + K_{CO}(CO)]^2} \quad (5)$$

where the K_{CO} represents the adsorption constants for CO (Step 1 in Scheme 1). In the context of the elementary steps depicted in Scheme 1, the value of γ is:

$$\gamma = K_{H_2} K_{HCO} k_{HCOH} \quad (6)$$

where K_{H2} is the adsorption constant for H_2 (Step 2), K_{HCO} is the CH*O* formation equilibrium constant (Step 3) and k_{HCOH} is the rate constant for CH*OH* formation (Step 4). High CO* coverages prevail at FTS conditions, resulting in $K_{CO}(CO) \gg 1$ and:

$$r = \frac{\gamma(H_2)}{K_{CO}^2(CO)} \quad (7)$$

where γ and K_{CO} can be written in terms of free energy differences as:

$$\frac{\gamma}{K_{CO}^2} = \frac{k_B T}{h} e^{\left(-\frac{\Delta G^{\ddagger}}{RT}\right)} \quad (8)$$

with

$$\Delta G^{\ddagger} = \Delta G_{\gamma}^{\ddagger} - \Delta G_{ads,CO} \quad (9)$$

$$\Delta G_{\gamma}^{\ddagger} = \Delta G_{act,4} + \Delta G_{rxn,3} + \Delta G_{ads,H_2} \quad (10)$$

These equations can be rewritten in terms of the free energies of CH*O*–H‡ and CO* and of gaseous species:

$$\Delta G_{\gamma}^{\ddagger} = G[CH^*O{-}H^{*\ddagger}] - G[H_2] - G[CO^*] - G[^*] \quad (11)$$

$$\Delta G_{ads,CO} = G[CO^*] - G[^*] - G[CO] \quad (12)$$

$\Delta G_{\gamma}^{\ddagger}$ thus represents the free energy of formation of the CH*O–H*‡ transition state from a surface with a single vacancy (along with the stoichiometric amounts of gaseous H_2).

Fig. 3 depicts the DFT-derived reaction coordinate with reaction and activation enthalpies and free energies for H-assisted CO*-activation routes. CO* desorption forms a vacant site (reverse of Step 1) with $-\Delta H_{ads,CO}$ and $-\Delta G_{ads,CO}$ values of 104 and 22 kJ mol^{-1}, respectively. Hydrogen is activated at this vacancy (Step 3) to form 2H′ species, one of which reacts with CO* to form CH*O* (which occupies two sites on the catalyst surface, Step 3) in an endothermic step (ΔH_{rxn} = +79 kJ mol^{-1}, ΔG_{rxn} = +82 kJ mol^{-1}). The barriers for CH*O* decomposition to H′ and CO* (reverse of Step 2, Scheme 1) are smaller (by 45 kJ mol^{-1} in enthalpy and by 78 kJ mol^{-1} in free energy) than for CH*O* reactions with H* to form CH*OH* (Step 4), thus rendering Step 3 quasi-equilibrated. The formation of CH_2O from CH*O* and H′ has $\Delta G^{\ddagger}$ of 226 kJ mol^{-1}, slightly lower than that to form CH*OH*. The reverse free energy

Table 1
Differential adsorption enthalpies (kJ mol^{-1}), Gibbs free energies (kJ mol^{-1}), and entropies (J mol^{-1} K^{-1}) for CO* on bare and CO*-saturated (1.044 ML) low-index terraces of Ru_{218} particles calculated using different functionals.

Functional	Potentials	0.004 ML CO*[a]			1.044 ML CO*[a]		
		ΔH (kJ mol^{-1})	ΔG (kJ mol^{-1})	ΔS (J mol^{-1} K^{-1})	ΔH (kJ mol^{-1})	ΔG (kJ mol^{-1})	ΔS (J mol^{-1} K^{-1})
RPBE	PAW	−151	−79	−144	−46	36	−165
RPBE-D3(NMI)	PAW	−151	−79	−144	−104	−22	−165
RPBE-D3	PAW	−193	−121	−144	−169	−87	−165
optB86b-vdW	PAW	−191	−120	−142	−138	−55	−165
vdW-DF2	PAW	−141	−70	−142	−67	13	−160
PBE	PAW	−175	−104	−142	−126	−45	−163
PW-91	USPP	−178	−100	−155	−96	−18	−156

[a] Coverages calculated based on 1 and 284 CO* species on full Ru_{586} nanoparticle cluster model.

$$CO + * \rightleftharpoons CO^* \quad (1)$$

$$H_2 + * \rightleftharpoons 2\,H' + * \quad (2)$$

$$CO^* + * + H' \rightleftharpoons HC^*O^* \quad (3)$$

$$HC^*O^* + H' \longrightarrow CH^*OH^* \quad (4)$$

$$CH^*OH^* \longrightarrow CH^* + OH^* \quad (5)$$

$$CH^* + OH^* + H' \longrightarrow CH^* + H_2O + * \quad (6)$$

Scheme 1. Mechanism for H-assisted CO* activation via CH*OH* intermediates, where * indicates a site which CO* can occupy and ′ indicates a three-fold site in which H′ can bind without concomitant CO* desorption.

barrier (158 kJ mol^{-1}) for CH_2O decomposition indicates that CH_2O is likely in equilibrium with CO and H_2. The equilibrium concentration of CH_2O will be very low at FTS conditions as the equilibrium constant is 9×10^{-5}, consistent with the presence of CH_2O as a trace product during FTS. The transition states for CH*OH* formation and for its dissociation (to CH* and OH*) exhibit similar formation enthalpies ($\Delta H^{\ddagger}$ = 234 and 233 kJ mol^{-1}, respectively) and free energies ($\Delta G^{\ddagger}$ of 228 kJ mol^{-1} and 225 kJ mol^{-1}, respectively). The similarities in these barriers make it impossible to determine the reversibility of CH*OH* formation. These two transition states are, however, kinetically-indistinguishable and lead to the same rate equation because of their similar stoichiometry; thus, the reversibility of CH*OH* formation does not affect the form of the observed rate equation (Eq. (8)), but only the mechanistic interpretation of γ. CH*OH* dissociation forms CH* and OH* and the latter reacts with H′ to form H_2O, which desorbs from the surface creating a vacant site for CO to adsorb. The $\Delta G^{\ddagger}$ for CH*O–H* formation is 228 kJ mol^{-1}, which comprises a ΔG_{γ} of 206 kJ mol^{-1} and a $\Delta G_{ads,CO}$ value −22 kJ mol^{-1} (Fig. 3B). The overall reaction that converts CO* and 1.5 H_2 to CH* and H_2O is exothermic (ΔH_{rxn} = −23 and ΔG_{rxn} = −2 kJ mol^{-1}, Fig. 4) and once a chain has been initiated (via CH* formation), it can either terminate to form undesired CH_4 or grow via CO*- or CH_x*-insertion mechanisms.

3.3. The formation of carbon–carbon bonds via CH_x*-insertion

The dearth of chains on working surfaces and their fast growth [4] may reflect direct CO* insertion, which we consider in a later study. Alternatively, CH_x* monomers or growing RCH_x* chains may decrease the free energy of the transition state for H′ addition to CH*O* (referenced to its relevant precursor), specifically by avoiding the need to remove an additional CO* to form this transition state.

The ratio of the rate of chain growth (C–C bond formation) to chain initiation (CO* activation) is simply given by:

$$\frac{r_{growth}}{r_{init}} = \bar{n} - 1 \quad (13)$$

where ($\bar{n}$) represents the average number of C-atoms in the products formed; this value is typically >10 for practical Fischer–Tropsch synthesis. The rate of chain initiation is given by Eq. (5) in which γ is the lumped rate constant for

$$CO^* + {}^* + H_2 \rightarrow CH^*O^*{-}H^{\ddagger} \quad (14)$$

which ultimately leads to CH* species on the catalyst surface (Step 5 in Scheme 1). Once two CH* species are co-adsorbed, they can react to form a new C–C bond:

$$CH^* + CH^* \rightarrow CH^*CH^* \quad (15)$$

The intrinsic activation enthalpies and free energies (ΔH_{act} and ΔG_{act} of 88 and 94 kJ mol^{-1}, respectively, Fig. 5) are much smaller than the effective activation enthalpies and free energies for CO* activation (230 and 235 kJ mol^{-1}), indicating that CH_x*-insertion reactions are limited by the high activation free energies for forming vicinal CH_x* species, rather than the activation free energies for C–C bond formation.

Alternative CH_x*-insertion steps, such as the reactions of CH* with CH_2* or CH_3*, and the H′-addition steps that ultimately form olefin and paraffin products are currently being examined using the same theoretical approaches utilized herein as part of a separate study.

3.4. CO* activation on dense CO* monolayers disrupted by growing chains

The rate of chain-growth is not limited by C–C bond formation, as these steps occur readily among vicinal hydrocarbon chains and CH_x* monomers, as shown in Section 3.3. Instead, growth rates are limited by CO* activation (to form CH_x* monomers) at sites vicinal to growing chains (of length n)

$$CO^* + C_nH^*_{2n-1} + H_2 \rightarrow CH^*O^*{-}H^{\ddagger} + C_nH'_{2n-1} \quad (16)$$

where the vicinal chain (shown as CH* in Fig. 4F) and CH*O*–H‡ transition states (Fig. 4B) share a metal atom site on the catalyst

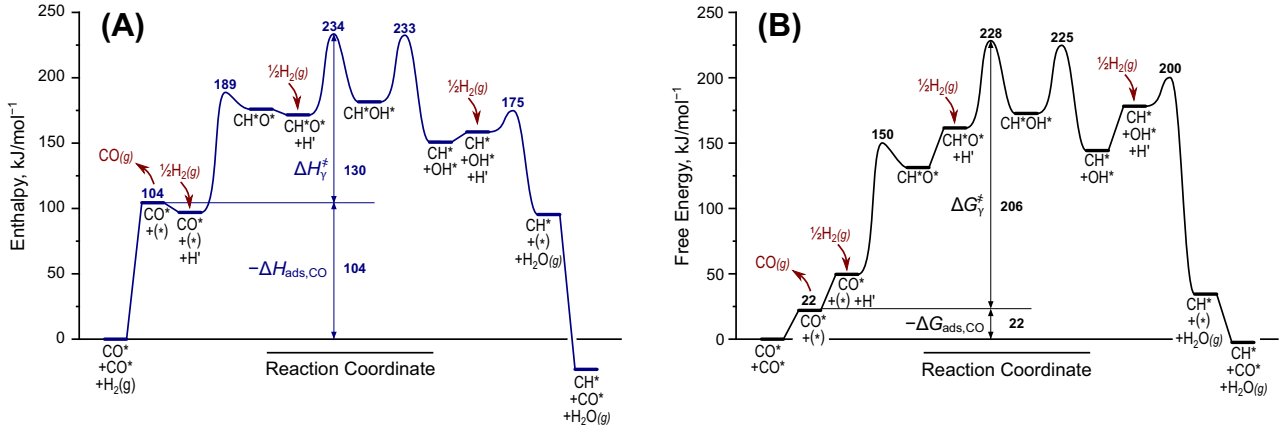

Fig. 3. (A) Enthalpy and (B) free energy diagrams for H*-assisted CO activation (chain initiation) on Ru_{218} nanoparticles at 1.04 ML CO*. Effective enthalpy and free energy barriers ($\Delta H^{\ddagger}$ and $\Delta G^{\ddagger}$ (Eq. (9))) reflect the ΔH and ΔG to form transition states from CO*-covered surfaces and stoichiometric amounts of H_2(g) and are shown for each transition state. $\Delta H^{\ddagger}_{\gamma}$ and $\Delta G^{\ddagger}_{\gamma}$ (Eq. (10)) represent the enthalpy and free energies to form the CH*O–H*‡ from CO* and a vicinal vacancy (*). Electronic energy differences and zero-point corrections are shown in the SI (Table S1).

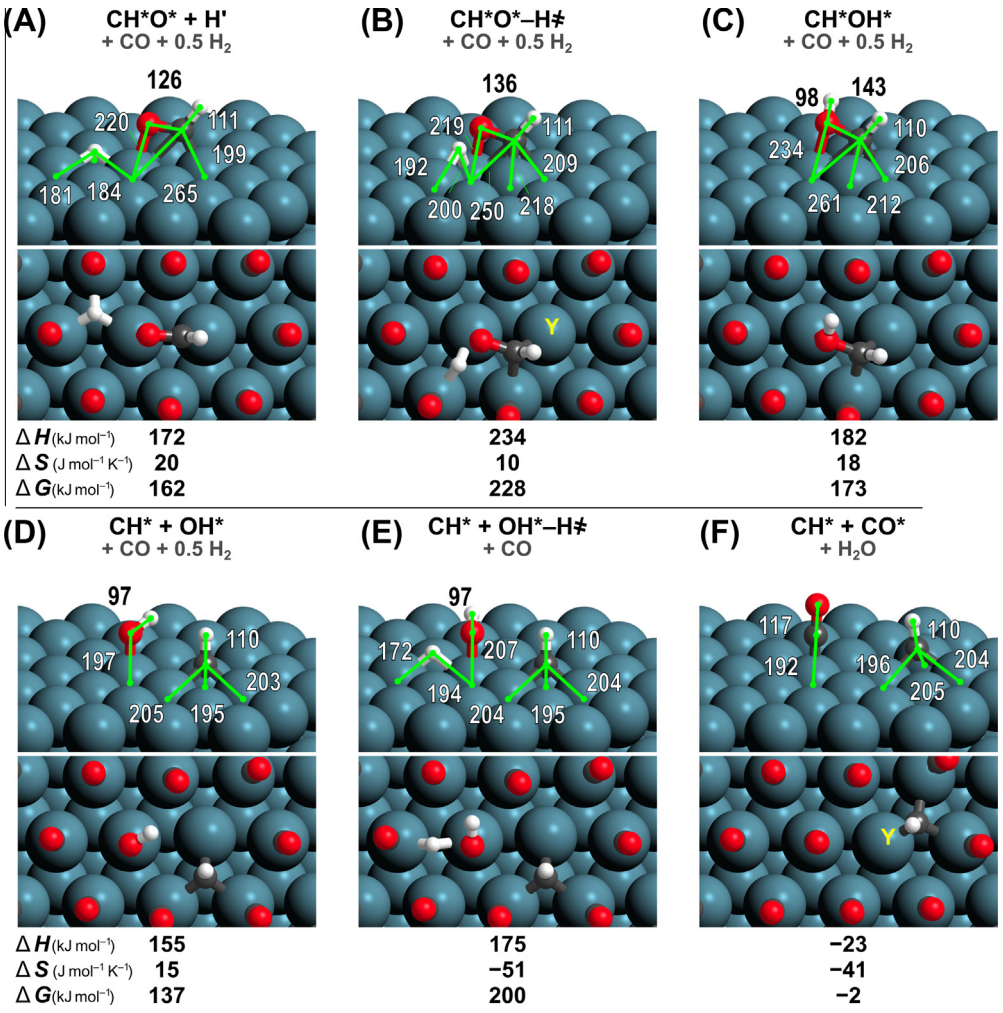

Fig. 4. DFT-derived structures for (A) CH*O* + H′, (B) CH*O*–H′, (C) CH*OH*, (D) CH* + OH*, (E) CH* + OH*–H′, and (F) CH* + CO* along with enthalpies, entropies and free energies to form those states (along with stoichiometric amounts of gas-phase species) from a CO*-covered surface. Top pictures omit spectating CO* species for clarity and have bond distances labeled in pm. Structures for all states in Fig. 3 shown in the SI (Figs. S1–S5).

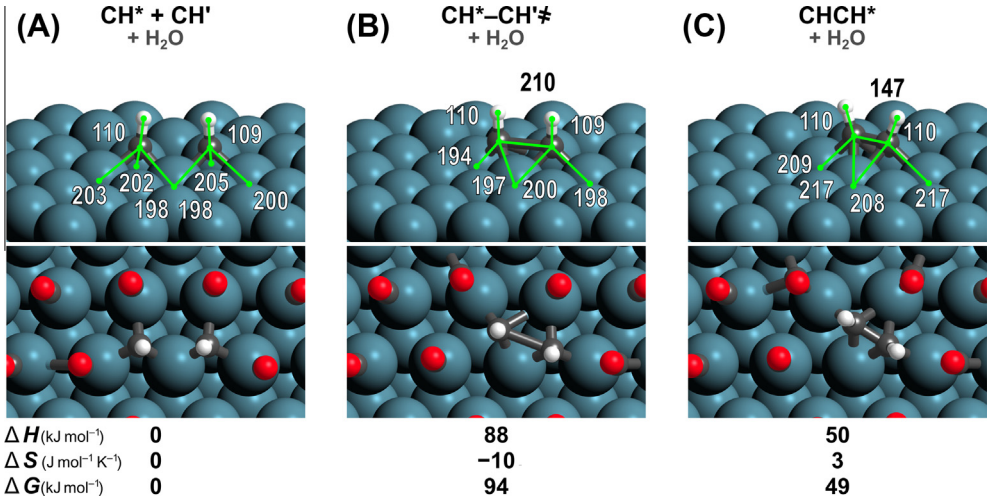

Fig. 5. DFT-derived structures for the (A) CH* + CH′, (B) CH*–CH′, and (C) CHCH* along with enthalpies, entropies and free energies to form the transition and product states from the reactant precursor. Top pictures omit spectating CO* species for clarity and have bond distances labeled in pm.

surface (labeled 'Y' in Fig. 4). The same sequence of elementary steps (Steps 2–6 in Scheme 1) leads to CH*O*–H‡ formation in Eqs. (14) and (16). The rate of chain growth (limited by Eq. (15)) can thus be written as:

$$r_{\text{growth}} = \frac{\gamma_n K_{\text{CO}}(\text{CO})(\text{H}_2)[C_n^*]}{1 + K_{\text{CO}}(\text{CO})} \tag{17}$$

where $[C_n^*]$ is the concentration of chains with length n. For each individual chain, Eqs. (5) and (17) can be rewritten as:

$$\frac{r_{\text{growth}}}{r_{\text{init}}[C_n^*]} = \frac{\gamma_n K_{\text{CO}}(\text{CO})}{\gamma_0} \tag{18}$$

at high CO pressures ($K_{\text{CO}}(\text{CO}) \gg 1$), where γ_0 and γ_n are the lumped rate constants for the steps in Eqs. (14) and (16). These γ parameters can be written in terms of free energy differences:

$$\gamma_i = \frac{k_B T}{h} \exp\left(\frac{-\Delta G_{\gamma i}}{RT}\right) \tag{19}$$

which can be rewritten in terms of the free energies of the CH*O*–H‡, CO*, and gas-phase species:

$$\Delta G_{\gamma 0}^{\ddagger} = G[\text{CH*O—H*}] - G[\text{H}_2] - G[\text{CO*}] - G[*] \tag{20}$$

$$\Delta G_{\gamma n}^{\ddagger} = G[\text{CH*O—H*}] - G[\text{H}_2] - G[\text{CO*}] - G[C_n^*] \tag{21}$$

These free energies are calculated from DFT with ($\Delta G_{\gamma n}^{\ddagger}$) and without ($\Delta G_{\gamma 0}^{\ddagger}$) a vicinal hydrocarbon chain.

First, we examine the activation of a CO* vicinal to a bound CH*. Fig. 4F shows that CH* binds to a three-fold site, preserving space in the CO*-monolayer on the catalyst surface directly above metal atom 'Y'. CO* adsorption at this site (Y) has a large positive $\Delta G_{\text{ads,CO}}$ (+21 kJ mol^{-1}), indicating that CO* adsorption is unlikely to occur, even at the typical CO pressures (10 bar) in FTS. This space in the CO*-monolayer above metal atom (Y), however, can accommodate the CH*O*–H‡ transition state, as discussed in the next section. Fig. 5 shows DFT-derived reaction and activation free energies for H-assisted CO* activation vicinal to CH* and for the H-assisted path within dense CO* monolayers without the disruptions by CH* species. The steps that initiate such chains within CO* monolayers require CO* desorption to create the space necessary to form and bind CH*O*–H‡ transition state structures, as discussed in Section 3.2. In contrast, CO* activation vicinal to a chain does not require CO* desorption, as the chain effectively prevents CO* adsorption at such nearby sites and preserves the vacancy. Except for the lack of this CO desorption requirement ($\Delta G_{\text{des,CO}}$ (+22 kJ mol^{-1})), the chain-assisted CO* activation proceeds via the same elementary steps as those for chain initiation on dense CO* monolayer surfaces (Steps 2–6 in Scheme 1). The free energy of activation to form CH*O*–H‡ from CO* and H_2 with a co-adsorbed CH* species ($\Delta G_{\gamma 1}^{\ddagger}$) is 204 kJ mol^{-1}, whereas the same reaction vicinal to a vacancy results in a similar value ($\Delta G_{\gamma 0}^{\ddagger}$ of 206 kJ mol^{-1}), leading to a decrease in the overall free energy barrier ($\Delta G^{\ddagger}$) of 24 kJ mol^{-1} for CH*-assisted CO* activation (Fig. 6). The small changes in $\Delta G_{\gamma}^{\ddagger}$ with co-adsorbed CH* ($\Delta G_{\gamma 1}^{\ddagger}$) and without a co-adsorbed CH* ($\Delta G_{\gamma 0}^{\ddagger}$) indicate that lateral interactions between CH*O*–H‡ and CH* are weak (<3 kJ mol^{-1}) as further demonstrated by similar CH*O*–H‡ geometries (Figs. 4B and 7B). The weak lateral interactions between CH* and the CH*O*–H‡ are unique to that reaction, as co-adsorbate interactions between CH* and the transition states for forming both CH*O* and H_2O* are significant, leading to similar $\Delta G^{\ddagger}$ values for those reactions during CH*-assisted and non-assisted paths. The rate of CO* activation, however, is ultimately dependent on the stabilities of the CH*O*–H‡ transition state, making these other transition states (or their interactions with vicinal chains) irrelevant to rates of CO* activation. The differences in the overall apparent activation energy for the non-assisted ($\Delta G_0^{\ddagger}$) (−24 kJ/mol) and the CH*-assisted ($\Delta G_1^{\ddagger}$) path (+24 kJ mol^{-1}) are predominantly due to the free energy required to desorb CO* ($\Delta G_{\text{des,CO}}$, +22 kJ mol^{-1}) to create the vacancy necessary to activate CO* on the non-assisted surface.

Furthermore, the difference between $\Delta G_0^{\ddagger}$ and $\Delta G_1^{\ddagger}$ was also computed for the optB86b-vdW functional (with PAW potentials) and the PW-91 functional (with USPP pseudopotentials) in order to benchmark the novel RPBE-D3(NMI) method presented here against more widely-used methods. The PW-91 functional predicted a difference between $\Delta G_0^{\ddagger}$ and $\Delta G_1^{\ddagger}$ of 30 kJ mol^{-1} while the optB86b-vdW method predicted a difference of 38 kJ mol^{-1} (Table S1, SI). The positive differences in free energy barriers by these methods are consistent with the difference (+24 kJ mol^{-1}) predicted by RPBE-D3(NMI), indicating that the conclusions herein are not dependent upon the choice of a unique functional. Furthermore, the differences between $\Delta G_0^{\ddagger}$ and $\Delta G_1^{\ddagger}$ for all three methods (24 kJ mol^{-1}, 30 kJ mol^{-1}, 38 kJ mol^{-1} for D3(NMI), PW-91, and optB86b-vdW) are similar to the $\Delta G_{\text{des,CO}}$ predicted by those methods (22 kJ mol^{-1}, 18 kJ mol^{-1}, and 55 kJ mol^{-1} for D3(NMI), PW-91, and optB86b-vdW) as shown in Fig. S10 (SI). This relationship between ($\Delta G_0^{\ddagger}$ and $\Delta G_1^{\ddagger}$) and $\Delta G_{\text{des,CO}}$ indicates that DFT methods which predict positive free energies for desorbing CO* (such as the widely-used PBE method, Table 1) will also predict positive

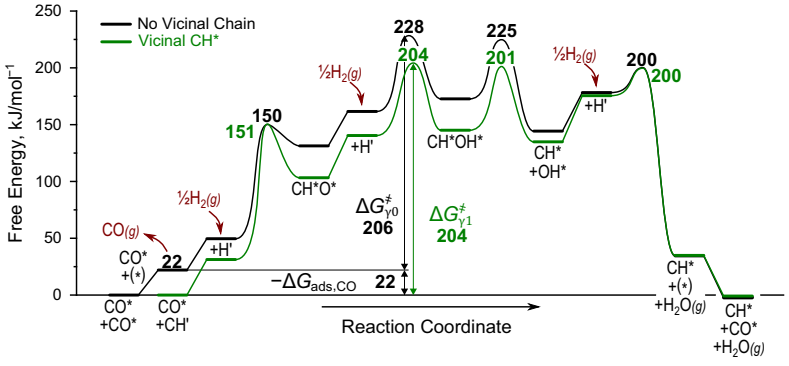

Fig. 6. Comparison of the free energy diagrams for the H*-assisted CO* activation without a vicinal chain (black curve) and the CH* promoted H*-assisted CO* activation (green curve) on Ru nanoparticles at 1.044 ML CO*. Effective free energy barriers ($\Delta G^{\ddagger}$) are the ΔG to form transition states from their respective 'reference' states and stoichiometric amounts of H_2 and are shown for each transition state. Labels for each state are simplified for clarity, but full labels can be seen in Fig. 3. Enthalpy differences (along with electronic energies and zero-point corrections) are shown in the SI (Tables S1 and S2).

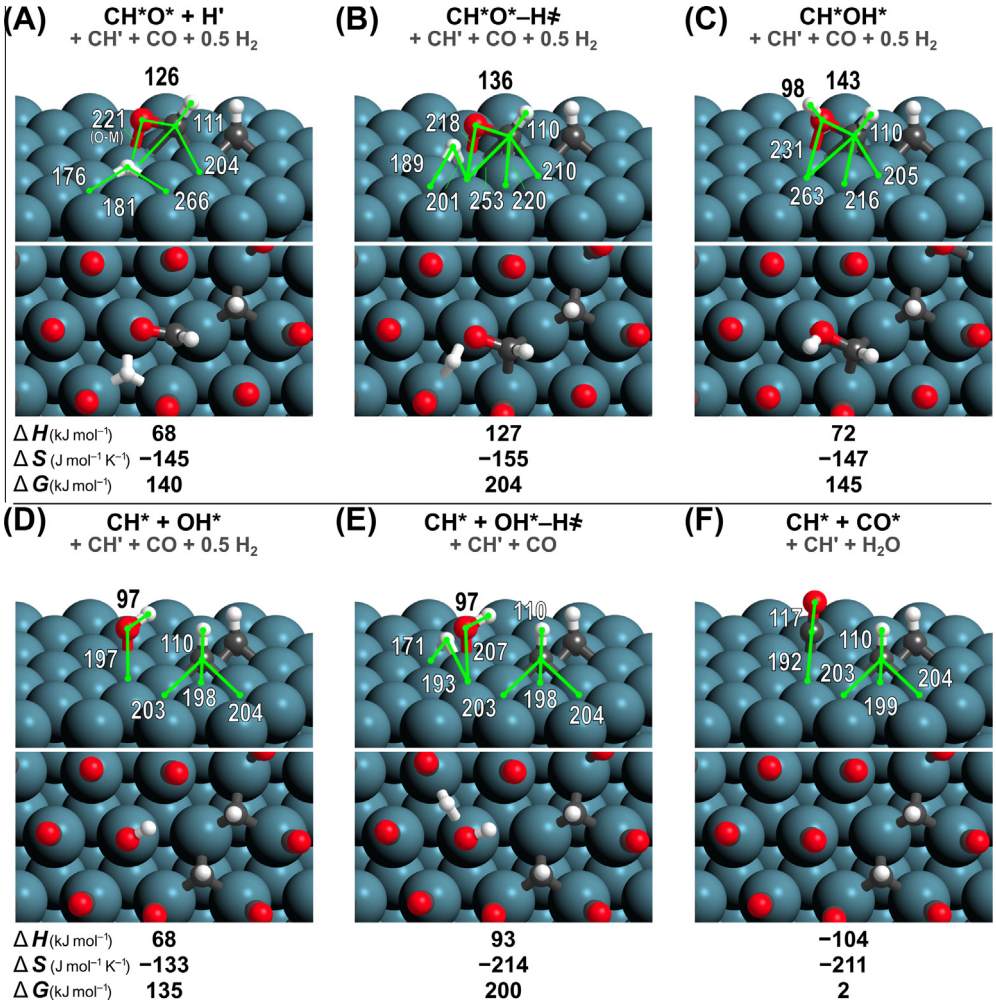

Fig. 7. DFT-calculated structures for (A) CH*O* + H′ + CH′, (B) CH*O*–H′ + CH′, (C) CH*OH* + CH′, (D) CH* + OH* + CH′, (E) CH* + OH*–H′ + CH′, and (F) CH* + CO* + CH′ along with enthalpies, entropies and free energies to form those states (along with stoichiometric amounts of gas-phase species) from CO* + CH* (Fig. 4F). Top pictures omit spectating CO* species for clarity and have bond distances labeled in pm. Structures for all states in Fig. 6 shown in the SI (Figs. S6–S9).

differences between $\Delta G_0^{\ddagger}$ and $\Delta G_1^{\ddagger}$, leading to conclusions consistent with those presented herein for the novel D3(NMI) approach.

To assess the effects of hydrocarbon chain length on the free energy barrier to form the CH*O*–H‡ transition state vicinal to a growing chain ($\Delta G_{\gamma i}^{\ddagger}$, $i > 0$), CO* activation was also examined vicinal to CH_3C^*, $C_2H_5C^*$, and $C_3H_7C^*$ (CO* activation vicinal to alkylidene and alkylidyne chains is discussed in Section 3.4). The average $\Delta G_{\gamma}^{\ddagger}$ for CH*O*–H‡ formation vicinal to an alkylidyne chain (C_1–C_4) is 213 kJ mol^{-1}, as shown in Fig. 8B, slightly higher than for CH* species ($\Delta G_{\gamma 1}^{\ddagger} = 206$ kJ mol^{-1}), leading to the ratio of lumped rate constants for CO* activation (γ_n/γ_0 in Eq. (18)) of ~0.2 at 500 K, which then simplifies to:

$$\frac{r_{\text{growth}}}{r_{\text{init}}[C_n^*]} = 0.2\,K_{\text{CO}}(\text{CO}) = 0.2\exp\left(\frac{-\Delta G_{\text{ads,CO}}}{RT}\right)(\text{CO}) \tag{22}$$

at high CO* coverages ($K_{\text{CO}}(\text{CO}) \gg 1$) inferred from experiments or estimated from DFT ($\Delta G_{\text{ads,CO}} = -22$ kJ mol^{-1}, Eq. (12)), resulting in large ratios of chain growth to chain initiation via CO* activation enhanced by vicinal hydrocarbon chains.

The ability of growing chains to promote the local activation of CO* leads to a rate equation modified from Eq. (5) to add CO* consumption vicinal to growing chains:

$$r_{\text{CO}} = \frac{\gamma_0 K_{\text{CO}}(\text{CO})(\text{H}_2)}{[1+K_{\text{CO}}(\text{CO})]^2}\left(1+\alpha_1\sum_{n=1}^{\infty}\left(\frac{\gamma_n}{\gamma_1}\right)\prod_{i=1}^{n}\alpha_{i-1}\right) \tag{23}$$

derived in the SI (by employing a pseudo-steady-state hypothesis on C_1^*, Eqs. (S14)–(S26)), where α is the chain growth probability:

$$\alpha_i = \frac{r_{\text{growth},i}}{r_{\text{growth},i} + r_{\text{term},i}} \tag{24}$$

The summation term in Eq. (23) represents CO*-consumed in the propagation of a chain (rather than in its initiation). At FTS conditions, this term is thus much greater than 1 (since chains are longer than C_{10} on average), indicating that most CO* is consumed at sites vicinal to growing chains, rather than on unperturbed CO*-covered surfaces as these chains are unable to migrate on CO*-covered surfaces. As a result, measured FTS activation barriers do not represent enthalpies of isolated CO* activation that initiate each chain (234 kJ mol^{-1}, Fig. 3A), but those for CO* activations vicinal to growing chains (average of 136 kJ mol^{-1}, Fig. 8A), whose values are similar to reported measured activation barriers (100–150 kJ mol^{-1}) on Co [7] and Ru [8] catalysts.

3.5. Relative alkylidyne, alkylidene, and alkyl coverages and their kinetic relevance

The results in Section 3.3 confirm that alkylidyne ($C_nH_{2n-1}^*$) species (e.g., CH*, CH_3C^*, $C_2H_5C^*$) promote the activation of vicinal CO* species on Ru surfaces by disrupting dense CO* adlayers and thus creating an activation space that avoids the need to desorb CO*. These surface alkylidyne are stable at high CO* coverages and do

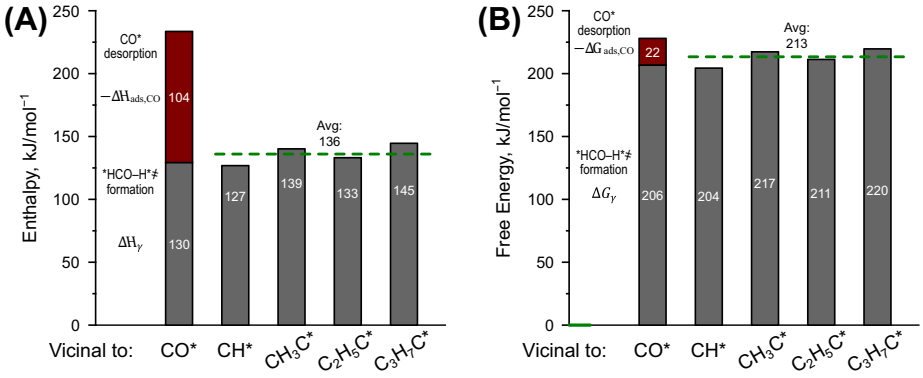

Fig. 8. (A) Enthalpy and (B) free energy differences (500 K) for forming CH*O*–H′ from CO* vicinal to a CO* ($\Delta H_{\gamma 1}$ and $\Delta G_{\gamma 1}$) and hydrocarbon chains ($C_nH_{2n-1}^*$, $\Delta H_{\gamma(n+1)}$ and $\Delta G_{\gamma(n+1)}$, n = 1–4). CO* desorption energies ($-\Delta H_{ads,CO}$ = 104 kJ mol^{-1} and $-\Delta G_{ads,CO}$ = 23 kJ mol^{-1}) are also shown as it is required for forming CH*O*–H′ from two CO* species on the surface (during initiation). The average $\Delta H_{\gamma n}$ and $\Delta G_{\gamma n}$ (n = 2–5) values (134 and 213 kJ mol^{-1}, respectively) are shown by the dashed line. Tables containing energies for the full H-assisted CO* activation pathways vicinal to a CO*, CH*, CH_3C^*, $C_2H_5C^*$, and $C_3H_7C^*$ are shown in the SI (Tables S2–S6).

not decompose which is consistent with previous studies [48] that show CO* block ethylidyne dehydrogenation paths and enhance its ability to react with other hydrocarbon surface intermediates. It seems plausible that other chemisorbed species, such as C*, alkylidenes ($C_nH_{2n}{}^*$), or alkyls ($C_nH_{2n+1}^*$) can also create such spaces and thus promote CO* activation in their vicinity.

The ratios of the rates of CO* activation vicinal to an alkylidene ($r_{CO,C_nH_{2n}^*}$) or alkyl $r_{CO,C_nH_{2n+1}^*}$) chain to that at a location vicinal to an alkylidyne chain ($r_{CO,C_nH_{2n-1}^*}$) are given by:

$$\frac{r_{CO,C_nH_{2n}^*}}{r_{CO,C_nH_{2n-1}^*}} = \frac{[C_nH_{2n}^*]}{[C_nH_{2n-1}^*]} \exp\left(\frac{-\Delta G_{\gamma,C_nH_{2n}^*} + \Delta G_{\gamma,C_nH_{2n-1}^*}}{RT}\right) \quad (25)$$

$$\frac{r_{CO,C_nH_{2n+1}^*}}{r_{CO,C_nH_{2n-1}^*}} = \frac{[C_nH_{2n+1}^*]}{[C_nH_{2n-1}^*]} \exp\left(\frac{-\Delta G_{\gamma,C_nH_{2n+1}^*} + \Delta G_{\gamma,C_nH_{2n-1}^*}}{RT}\right) \quad (26)$$

respectively. These ratios depend in turn on the relative coverages of alkylidene or alkyl chains to those of alkylidynes and on the difference in the respective free energy barriers to form CH*O–H*′ from CO* and H_2 ($\Delta G_\gamma^\prime$) at these various locations, as given by Eqs. (25) and (26). In assessing the contributions to CO activation at these different locations, we first consider the $[C_nH_{2n}{}^*]/[C_nH_{2n-1}^*]$ and $[C_nH_{2n+1}^*]/[C_nH_{2n-1}^*]$ coverage ratios for these C_1 species. CH* binds at three-fold sites (Fig. 4D) and can react with H′ (from quasi-equilibrated H_2 dissociation, Step 2 in Scheme 1) to form CH_2^*:

$$CH^* + H' \rightarrow CH_2^* \quad (27)$$

for which, the DFT-derived ΔH_{rxn} value is 51 kJ mol^{-1} and the ΔG_{rxn} value is 81 kJ mol^{-1} (500 K, 1 bar H_2). The assumption of quasi-equilibrium for Eq. (27) then leads to a maximum $[CH_2^*]/[CH^*]$ ratio that depends on $\Delta G_{rxn,27}$ and on the H_2 pressure [(H_2) in bar]:

$$\frac{[CH_2^*]}{[CH^*]} = e^{\left(\frac{-\Delta G_{rxn,27}}{RT}\right)}(H_2)^{0.5} \quad (28)$$

This ratio is ~10^{-8} at 10 bar H_2 and 500 K (Fig. 9). A similar analysis for the formation of CH_3^* via CH_2^* reactions with H′:

$$CH_2^* + H' \rightarrow CH_3^* \quad (29)$$

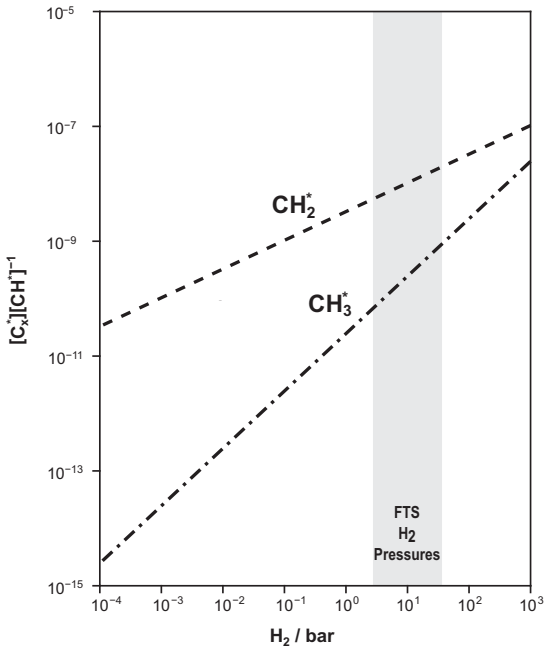

Fig. 9. Ratios of CH_2^* and CH_3^* to CH* at 500 K as a function of H_2 pressure (bar). H_2 pressures typical of FTS are shown in a shaded region.

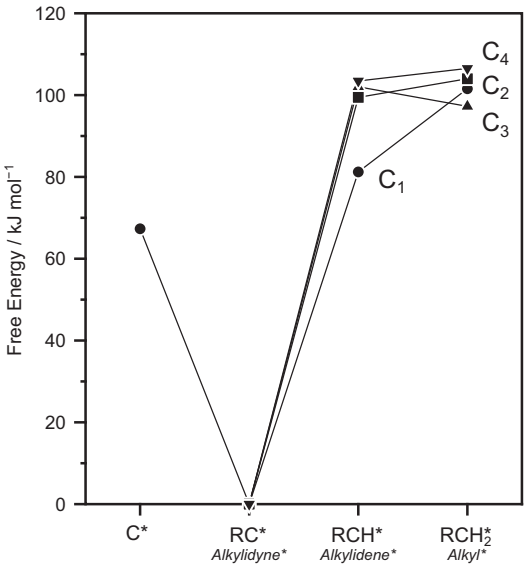

Fig. 10. Free energies (kJ mol^{-1}, 500 K, 1 bar H_2) to form alkylidene (RCH*, R = H, CH_3, C_2H_5, C_3H_7) and alkyl (RCH_2^*) species from C1–C4 alkylidynes (RC*) (C_1: ●, C_2: ■, C_3: ▲, C_4: ▼) and a stoichiometric amount of H_2. Also shown is the free energy to form C* (and ½H_2(g)) from CH*.

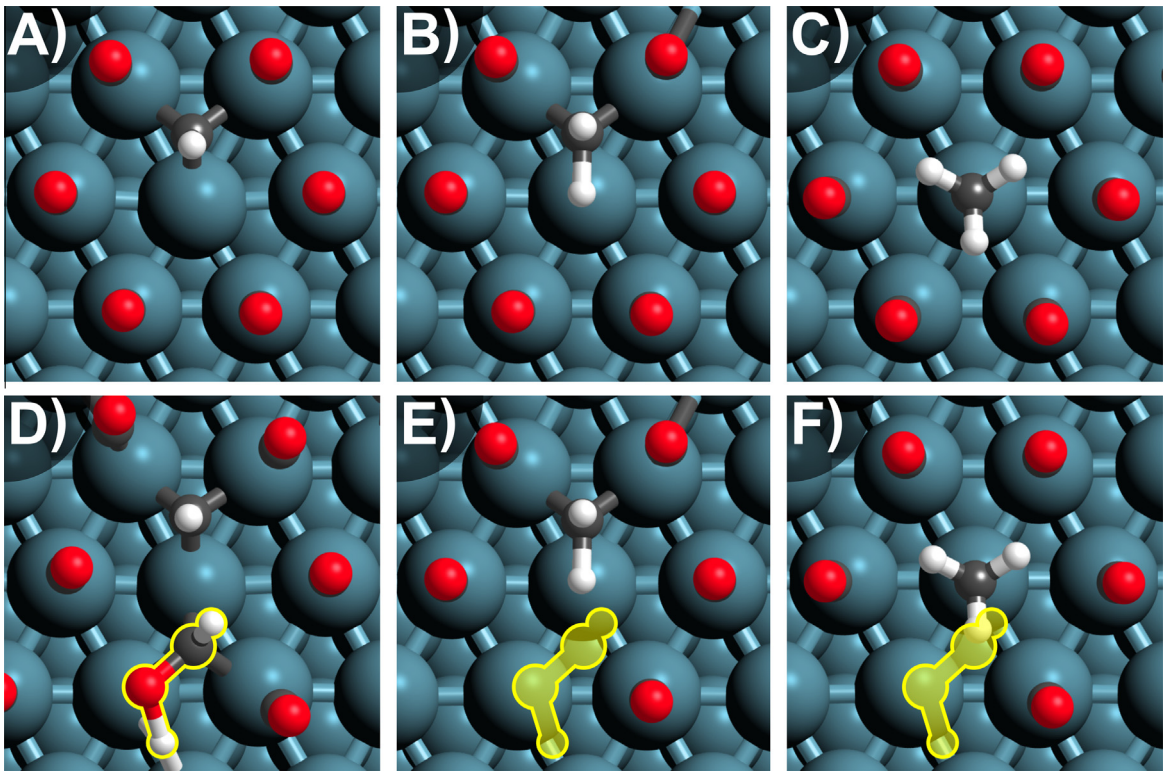

Fig. 11. (A)–(D) DFT-calculated structures of CH*, CH_2^*, CH_3^*, and the *CHO–H*′ transition state vicinal to a CH*. (E)–(F) Overlays of DFT-calculated structures for CH_2^* and CH_3^* with the *CHO–H*′ transition state from (D).

gives a maximum $[CH_3^*]/[CH^*]$ ratio when equilibrated:

$$\frac{[CH_3^*]}{[CH^*]} = e^{\left(\frac{-\Delta G_{rxn,29} - \Delta G_{rxn,27}}{RT}\right)}(H_2) \quad (30)$$

This value is $\sim 10^{-10}$ at 10 bar H_2 and 500 K (Fig. 9). These very low concentrations of CH_2^* and CH_3^* relative to CH* reflect the large ΔG_{rxn} of Eqs. (27) and (29) (81 and 18 kJ mol^{-1} at 500 K, 1 bar H_2).

The small concentrations of CH_2^* and CH_3^* relative to CH* reflect their large ΔH_{rxn} (51 and 46 kJ mol^{-1}, respectively) and ΔG_{rxn} (81 and 102 kJ mol^{-1}, respectively) (500 K) for their formation from CH* and the stoichiometric amount of H_2 (Fig. 10). The ΔG_{rxn} values for the corresponding formation of C_2–C_4 alkylidenes from alkylidynes (and ½H_2(g)) are 99, 102, and 103 kJ mol^{-1}, respectively, and thus even larger than for similar reactions of C_1^* species (by ~20 kJ mol^{-1}; Fig. 10); the ΔG_{rxn} values for the formation of C_2–C_4 alkyls from alkylidynes are 104, 97, and 107 kJ mol^{-1}, respectively, and thus similar to those for the respective C_1^* species (102 kJ mol^{-1}, 500 K; Fig. 10). These ΔG_{rxn} values indicate that alkylidynes are also the predominant C_2–C_4 species present as growing chains on Ru surfaces. At all conditions relevant to FTS practice, they represent the most abundant form of adsorbed chains, with alkyls and alkylidenes present as minor species (Eqs. (25) and (26); Fig. 9). These relative abundancies cast doubt upon C–C bond formation through alkylidene insertions into alkyl chains suggested in the literature [19,20,50,51], in favor of growth via alkylidyne species, as suggested elsewhere [22–25].

In light of these relative coverages, the free energy barriers to form CH*O–H*′ (ΔG_γ^i) near alkylidene and alkyl chains would have to be ~100 kJ mol^{-1} lower than the free energy barriers for forming CH*O–H*′ near alkylidyne species for the CO* activation near alkylidene or alkyl chains to contribute to chain growth. First, we note that the ΔG_γ^i for CO* activation near vacancies (207 kJ mol^{-1}) was similar to that near C_1–C_4 alkylidyne chains (average of 213 kJ mol^{-1}), indicating that the effects of co-adsorbates on ΔG_γ^i are generally weakly repulsive. Furthermore, the binding modes of alkylidene and alkyl species (shown in Fig. 11B and 11C for C_1 species) would lead to greater interference between those chains and CH*O–H*′ (shown by a yellow-shaded overlay in Fig. 11E and 11F), in contrast to CH*O–H*′ formation near CH* (Fig. 11D). Alkylidyne chains are the most abundant form of growing chains on the catalyst surface (Fig. 9) and they effectively disrupt CO*-adlayers to facilitate further activations of CO* species and thus rapidly increase the rate of chain growth over that of chain initiation.

4. Conclusions

Chains grow much more rapidly than they initiate during FTS on Ru and Co surfaces, which appears inconsistent with chain growth via CH_x^*-insertion (carbene-like) mechanisms as CH_x^* species have to be created via CO* activation processes identical to those which initiate chains. Here, this inconsistency is resolved through the use of DFT calculations at the high CO* coverages (1.044 ML) relevant to FTS by demonstrating that alkylidyne hydrocarbon chains ($C_nH_{2n-1}^*$, $n = 1$–4) disrupt the CO* adlayer and permit H-assisted CO* activation without CO* desorption, leading to activation enthalpies and free energies ~100 and ~15 kJ mol^{-1} lower for CO* activation near chains than within unperturbed monolayers. Alkylidyne species are much more abundant (by $\sim 10^8$) than alkylidene or alkyl species which do not permit CO* activation at vicinal sites. Once formed, CH* species can easily form C–C bonds with hydrocarbon chains (activation free energies <100 kJ mol^{-1}), ultimately leading to observed alkene and alkane products. Co follows the same rate law and displays similar product distributions and measured activation barriers as Ru, indicating that the mechanism for FTS is likely similar on both metals. Thus, we consider the

ability of CO* to activate more rapidly near chains to be applicable to both metals.

Acknowledgments

The authors acknowledge the financial support and computational resources provided by BP through the X-Conversion Consortium (BP-XC^2). We thank Drs. Craig Plaisance, Corneliu Buda, Jay Labinger, John Shabaker, and George Huff for helpful technical discussions. Computational resources were also provided by the Molecular Science Computing Facility (MSCF) in the William R. Wiley Environmental Molecular Sciences Laboratory, a national scientific user facility sponsored by the U.S. Department of Energy, Office of Biological and Environmental Research at the Pacific Northwest National Laboratory.

Appendix A. Supplementary material

Supplementary data associated with this article can be found, in the online version, at http://dx.doi.org/10.1016/j.jcat.2016.01.010.

References

[1] F. Fischer, H. Tropsch, Brennstoff-Chemie Bd 7 (1926) 97–116.
[2] E. Iglesia, Appl. Catal. A: Gen. 161 (1997) 59–78.
[3] M. Vannice, Catal. Rev. Eng. 14 (1976) 153–191.
[4] C.A. Mims, L.E. McCandlish, J. Phys. Chem. 91 (1987) 929–937.
[5] R.S. Dixit, L.L. Tavlarides, Ind. Eng. Chem. Process Des. Dev. 22 (1983) 1–9.
[6] M. Ojeda, R. Nabar, A.U. Nilekar, A. Ishikawa, M. Mavrikakis, E. Iglesia, J. Catal. 272 (2010) 287–297.
[7] I.C. Yates, C.N. Satterfield, Energy Fuels 5 (1991) 168–173.
[8] B.T. Loveless, C. Buda, M. Neurock, E. Iglesia, J. Am. Chem. Soc. 135 (2013) 6107–6121.
[9] P. Winslow, A.T. Bell, J. Catal. 86 (1984) 158–172.
[10] D.D. Hibbitts, B.T. Loveless, M. Neurock, E. Iglesia, Angew. Chem. Int. Ed. Engl. 52 (2013) 12273–12278.
[11] M. Ojeda, A. Li, R. Nabar, A.U. Nilekar, M. Mavrikakis, E. Iglesia, J. Phys. Chem. C 114 (2010) 19761–19770.
[12] O.R. Inderwildi, S.J. Jenkins, D.A. King, J. Phys. Chem. C 112 (2008) 1305–1307.
[13] H. Pichler, H. Schulz, Chem. Ing. Tech. 42 (1970) 1162.
[14] M. Zhuo, K.F. Tan, A. Borgna, M. Saeys, J. Phys. Chem. C 113 (2009) 8357–8365.
[15] Y.H. Zhao, K. Sun, X. Ma, J. Liu, D. Sun, H.Y. Su, W.X. Li, Angew. Chem. Int. Ed. 50 (2011) 5335–5338.
[16] M. Zhuo, A. Borgna, M. Saeys, J. Catal. 297 (2013) 217–226.
[17] B. Todic, W. Ma, G. Jacobs, B.H. Davis, D.B. Bukur, Catal. Today 228 (2014) 32–39.
[18] R.A. van Santen, A.J. Markvoort, ChemCatChem 5 (2013) 3384–3397.
[19] R. Brady, R. Pettit, J. Am. Chem. Soc. 102 (1980) 6181–6182.
[20] R.C. Brady, R. Pettit, J. Am. Chem. Soc. 103 (1981) 1287–1289.
[21] C.A. Mims, L.E. McCandlish, M.T. Melchior, Catal. Lett. 1 (1988) 121–125.
[22] I.M. Ciobîcă, G.J. Kramer, Q. Ge, M. Neurock, R.A. van Santen, J. Catal. 212 (2002) 136–144.
[23] Z.-P. Liu, P. Hu, J. Am. Chem. Soc. 124 (2002) 11568–11569.
[24] M.L. Turner, N. Marsih, B.E. Mann, R. Quyoum, H.C. Long, P.M. Maitlis, J. Am. Chem. Soc. 124 (2002) 10456–10472.
[25] J. Cheng, P. Hu, P. Ellis, S. French, G. Kelly, C.M. Lok, J. Phys. Chem. C (2008) 6082–6086.
[26] P.M. Maitlis, V. Zanotti, Catal. Lett. 122 (2008) 80–83.
[27] G. Kresse, J. Hafner, Phys. Rev. B 47 (1993) 558–561.
[28] G. Kresse, J. Hafner, Phys. Rev. B 49 (1994) 14251–14269.
[29] G. Kresse, J. Furthmüller, Phys. Rev. B Condens. Matter Mater. Phys. 54 (1996) 11169–11186.
[30] G. Kresse, J. Furthmüller, Comput. Mater. Sci. 6 (1996) 15–50.
[31] P. Blöchl, Phys. Rev. B 50 (1994) 17953–17979.
[32] G. Kresse, D. Joubert, Phys. Rev. B Condens. Matter Mater. Phys. 59 (1999) 11–19.
[33] J. Perdew, K. Burke, M. Ernzerhof, Phys. Rev. Lett. 77 (1996) 3865–3868.
[34] Y. Zhang, W. Yang, Phys. Rev. Lett. 80 (1998) 890.
[35] B. Hammer, L. Hansen, J.K. Nørskov, Phys. Rev. B Condens. Matter Mater. Phys. 59 (1999) 7413–7421.
[36] J. Klimeš, D. Bowler, A. Michaelides, Phys. Rev. B 83 (2011) 1–13.
[37] K. Lee, D. Murray, L. Kong, B.I. Lundqvist, D.C. Langreth, É.D. Murray, L. Kong, B. I. Lundqvist, D.C. Langreth, Phys. Rev. B 82 (2010) 081101(R).
[38] S. Grimme, J. Antony, S. Ehrlich, H. Krieg, J. Chem. Phys. 132 (2010) 154104.
[39] S. Grimme, S. Ehrlich, L. Goerigk, J. Comput. Chem. 32 (2011) 1456–1465.
[40] H. Monkhorst, J. Pack, Phys. Rev. B 13 (1976) 5188–5192.
[41] J. Liu, D. Hibbitts, E. Iglesia, 2016 (submitted for publication).
[42] D.E. Starr, H. Bluhm, Surf. Sci. 608 (2013) 241–248.
[43] H. Jonsson, G. Mills, H. Jónsson, K.W. Jacobsen, Class. Quant. Dynam. Condens. Phase Simul. – Proc. Int. Sch. Phys. (1998) 385–404.
[44] G. Henkelman, H. Jónsson, H. Jo, J. Chem. Phys. 113 (2000) 9978 (I. Introduction).
[45] G. Henkelman, H. Jónsson, J. Chem. Phys. 111 (1999) 7010.
[46] J.P. den Breejen, P.B. Radstake, G.L. Bezemer, J.H. Bitter, V. Frøseth, A. Holmen, K.P. de Jong, J. Am. Chem. Soc. 131 (2009) 7197–7203.
[47] J.M.G. Carballo, J. Yang, A. Holmen, S. García-Rodríguez, S. Rojas, M. Ojeda, J.L. G. Fierro, J. Catal. 284 (2011) 102–108.
[48] M. Gajdo, A. Eichler, J. Hafner, J. Phys.: Condens. Matter 16 (2004) 1141–1164.
[49] F. Abild-Pedersen, M.P. Andersson, Surf. Sci. 601 (2007) 1747–1753.
[50] E. van Steen, H. Schulz, Appl. Catal. A: Gen. 186 (1999) 309–320.
[51] H. Schulz, E. vein Steen, M. Claeys, Stud. Surf. Sci. Catal. 81 (1994) 455–460.